Journal Name

Dynamic Article Links ►

Cite this: DOI: 10.1039/c0xx00000x

www.rsc.org/xxxxxx

ARTICLE TYPE

Embedding catalytic nanoparticles inside mesoporous structures with controlled porosity: Au@TiO_2

Raquel Nafria,[a] Pilar Ramírez de la Piscina,[b] Narcís Homs,[a,b] Joan Ramón Morante,[a,c] Andreu Cabot,[a,c] Urbano Diaz,[d] Avelino Corma*[d]*

Received (in XXX, XXX) Xth XXXXXXXXX 20XX, Accepted Xth XXXXXXXXX 20XX
DOI: 10.1039/b000000x

The hability to produce catalytic nanoparticles with controlled properties is key to develop and produce heterogeneous catalysts with optimized activity and selectivity. Not less important is to maximize the nanoparticle dispersion over high area supports maintaining their optimized properties. Here we detail a general procedure to produce heterogeneous catalysts containing a large surface area mesoporuos support and highly dispersed catalytic nanoparticles with controlled properties. We exemplify the developed method using colloidal gold nanocrystals as the catalytically active phase and titanium oxide as the paradigmatic support. Our synthetic strategy is based on the formation of an inorganic-organic hybrid mesoporous material from the surface of the colloidal nanocrystals. A variety of organic spacers allows tuning the final porosity of the support. The good accessibility of the active catalytic sites in these materials is demonstrated by high CO oxidation conversion values.

Introduction

When preparing heterogeneous catalysts formed by metal nanoparticles dispersed on high area oxide supports, one aims to maximize the nanoparticle dispersion and its most active and selective facets, to optimize its size, and in some cases to enhance the interaction strength between the metal nanoparticle and the oxide support. A first step towards maximizing the active phase dispersion is the use of mesoporous supports with large surface areas. The challenge arrives when attempting to disperse the active catalytic phase in such highly porous structures. Conventional impregnation methods hardly allow to take full advantage of the enormous surface areas of mesoporous supports. Moreover, impregnation methods do not provide the level of control over the nanoparticle properties required to optimize their catalytic performance. A solution towards optimizing nanoparticle properties can be found in colloidal synthesis routes, which have been demonstrated successful in preparing nanoparticles with a high level of control over size, geometry, phase, and composition.[1-5] However, the dispersion of these nanoparticles over oxide supports, especially those with large surface areas and small pores is an extremely challenging task.

Recently, a new synthetic strategy to produce mesoporous silica matrices with embedded but accessible gold nanoparticles has been reported.[1,6-9] This strategy involves the formation of three-component metal-organic-inorganic structures by means of the polymerization of organosilica units anchored at the surface of colloidal metal nanoparticles.

In the present study, we generalize this synthetic procedure to the preparation of dispersed and accessible metal nanoparticles embedded within transition metal mesoporous matrices having controlled porosity. We exemplify the method using colloidal gold nanocrystals as the active catalytic phase and titanium oxide as the model support. Aromatic carboxylates derivates were used as physical spacers between titanium centers in the initial inorganic-organic hybrid framework [10-12]. We demonstrate the accessibility of the catalytic nanoparticles embedded in TiO_2 mesoporous matrices by measuring the CO oxidation at low temperature and analyzing the coordination sites by means of DRIFT spectroscopy.

Experimental section

Preparation of gold nanoparticles: Gold nanoparticles were prepared following the procedure reported by Budroni and Corma.[6,7] In a typical synthesis, 0.2 ml H_2O, 23 ml isooctane and 1 g sodium bis(2-ethylhexyl)sulfosuccinate (AOT) were stirred for 20 min. Then, 1.2 ml of a 0.1 M $HAuCl_4$ aqueous solution was added to the emulsion. After 15 min stirring, a mixture of 55.7 µl 1-dodecanethiol (DT) and 3.4 µl mercaptopropyltrimethoxysilane (MPMS) was added. Then, 100 µl of hydrazine was injected to reduce the gold ions into metallic gold nanocrystals. After 3 hours of stirring, the solution was left to rest overnight. The precipitate was separated from the clear

solution by decantation. Nanoparticles were filtered using a Whataman nylon membrane 0.45 μm, washed with toluene, and finally re-dispersed using an ultrasonic bath.

Preparation of gold-titania mesoporous structures, Au@TiO_2: 40 ml of a solution containing Au nanoparticles in ethanol ($3 \cdot 10^{-3}$ M) prepared following the previous procedure, were added to a solution containing 6.9 ml of titanium (IV) ethoxide and 1 ml of H_2O. After stirring during 30 minutes at room temperature, the solution became a gel that slowly converted into a white powder. The obtained powder was dried overnight at 100 ^oC in a vacuum oven and afterward calcined in air at 450 ^oC for 4 hours to remove the remaining organic molecules.

Preparation of gold-spacer-titania mesoporous structures, Au@TiO_2 (x): 11 ml of a toluene solution containing Au nanoparticles (0.01 M) prepared following the above procedure were added to a solution containing 2.6 ml titanium (IV) ethoxide and 47 μl of H_2O. This mixture was then added to 100 ml of a diethylformamide solution containing the appropriate amount of the selected carboxylic acid (molar ratio $Ti(OEt)_4$)/carboxylic acid = 1.35). The concentration of the organic spacer was selected taking into account the results obtained in a previous work.[10] The final solution was vigorously stirred and heated to 120 ^oC under Ar for 12 h. The gel-like precipitate obtained was filtered and washed with toluene. The precipitate was dried in a vacuum oven for 48 h at 160 ^oC. Temperature was afterward raised to 180 ^oC and maintained there for 6 h. The obtained powder was calcined in air at 450 ^oC for 4 h to remove organic molecules.[10] Scheme 1 represents the synthesis method. Table 1 details the carboxylic acid used and the nomenclature of the gold-spacer-titania mesoporous structure prepared.

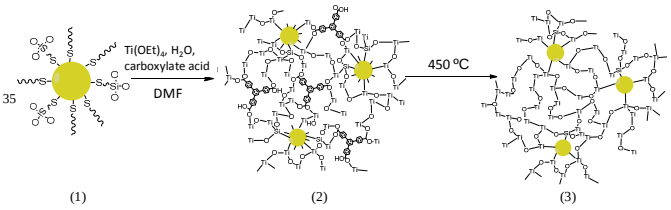

Scheme 1. Synthesis procedure. 1) gold nanoparticles stabilized with 1-dodecanethiol (DT) and mercaptopropyltrimethoxysilane (MPMS); 2) hybrid organic-inorganic network containing the gold nanoparticles and using 1,3,5-Tris(4-carboxyphenyl)benzene as the physical spacer; 3) final mesoporous matrices Au@TiO_2.

Materials characterization:

Crystallographic phases were characterized using powder x-ray diffraction (XRD). XRD patterns were obtained on a Bruker D8 automated diffractometer, equipped with a primary monochromator and LynxEye detector and using Cu Kα radiation. The instrument resolution was 0.05 ^{o} in 2θ, the studied range was from 4-80^o and the acquisition time for each sample was set to 1 h 20 min.

The specific surface area of the materials was determined by N_2 adsorption at 77 K using a Tristar II 3020 Micromeritics system. Specific areas were calculated using the Brunauer- Emmet-Teller (BET) method. The BET specific surface area was obtained from the analysis of the adsorption at P/Po=0.999.

Thermogravimetric analyses (TGA) were performed in the temperature range 30-800 ^oC at a heating rate of 10 ^oC/min under air using a Perkin Elmer TGA4000.

Metal contents were determined using optical emission spectroscopy by means of inductively coupled plasma (ICP) on a Perkin Elmer Optima 3200 RL system.

Elemental analyses were performed using an elemental organic analyzer Thermo EA 1108, working under 120 ml/min helium flow, the combustion furnace at 1000 ^oC, the chromatografic column oven at 60 ^oC, and 10 ml oxygen loop at 100 kPa.

Transmission electron microscopy (TEM) micrographs were obtained using a JEOL JEM-2100.

FT-IR spectra were recorded on a Bruker IR ALPHA in the range 4000–400 cm^2.

Table 1. Nomenclature of the gold-spacer-titania mesoporous structures prepared.

Sample name	Carboxylate	Carboxylate structure
Au@TiO_2 (t)	Terephtalic acid	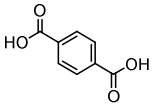
Au@TiO_2 (n)	2,6-Naphthalenedicarboxylic acid	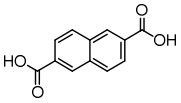
Au@TiO_2 (b)	1,3,5-Tris(4-carboxyphenyl)benzene	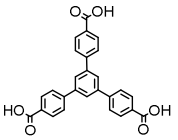

Catalytic activity:

Catalytic tests were carried out in a Microactivity-Reference unit (PID Eng&TECH) in the temperature range 25-250 ^oC under atmospheric pressure. 100 mg of catalyst was mixed with inactive SiC (Prolabo, 0.21 mm) and placed in a tubular fixed-bed reactor (305 mm long, 9 mm i.d., 316-L stainless steel) up to a catalytic volume of 0.5 ml. The temperature was measured by a thermocouple in direct contact with the catalytic bed. A mixture of 8.1 % CO, air (CO/O_2 molar ratio = 2, N_2 was used as a internal standard) and balanced with He, was feed to the reactor. A gas hourly space velocity (GHSV = volumetric inlet gas flow/catalyst volume bed) of 6700 h^{-1} was used. The products were analysed on-line with a Varian 450-GC gas chromatograph equipped with a methanizer and TCD and FID detectors.

Catalytic tests, related with the water gas shift (WGS) reaction, were carried out in the same equipment in the temperature range 250-450 ^oC under atmospheric pressure. 100 mg of catalyst was mixed with inactive SiC (Prolabo, 0.21 mm) and placed in a tubular fixed-bed reactor (305 mm long, 9 mm i.d., 316-L stainless steel) up to a catalytic volume of 0.5 ml. The temperature was measured by a thermocouple in direct contact with the catalytic bed. A mixture of 7.5 % CO, vapor (CO/H_2O

molar ratio = 2.6) and balanced with Ar was feed into reactor, using a GHSV =9965 h^{-1}.

The CO oxidation reaction was monitored by means of diffuse reflectance infrared spectroscopy (DRIFT) in a Nicolet Magna-IR 750 FTIR spectrometer equipped with a liquid-nitrogen-cooled MCT detector and a Spectra Tech Inc. catalytic DRIFT chamber. The outlet of the DRIFT chamber was connected on-line through a capillary tube to a Balzers instrument (QME 200) equipped with a quadrupole mass spectrometer, which had been previously calibrated to monitor the evolution of the different potential products. A mixture of 9.87 % CO/He and 10.03 % O_2/He in a molar ratio CO/O_2= 2 molar and balanced with He, in a total flow of 30 ml/min, was feed into the catalytic DRIFT chamber.

Results and discussions

Gold nanoparticles stabilized with DT and MPMS were produced following the procedure reported by Budroni and Corma.[6] A representative TEM micrograph of the Au nanoparticles and its corresponding size distribution histogram are displayed in Figure 1a. The average size of the gold nanoparticles prepared and used in this work was 2.1 ± 0.5 nm.

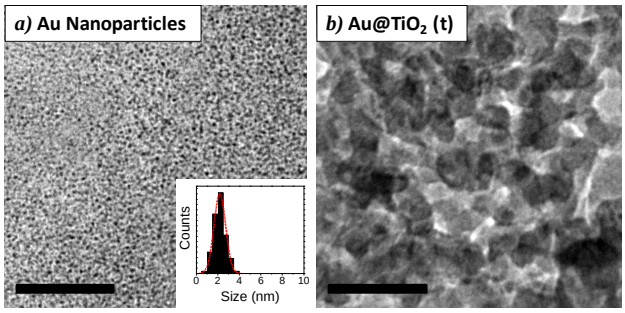

Figure 1. a) TEM micrographs of Au nanoparticles with average size of 2 nm. Inset shows the histogram of the particle size distribution. B) TEM micrograph of the calcined Au@TiO_2 (t) material. Scale bars correspond to 50 nm.

Au-organic-Ti materials were prepared from an ethanol solution of DT- and MPMS-caped Au nanoparticles and titanium (IV) ethoxide. Each surface ligand, DT and MPMS, plays a key role during the formation of the hybrid material. The MPMS alkoxysilane groups promote the hydrolysis and condensation of $Ti(OEt)_4$ around the gold NP and provide a link between the metal and the titania. On the other hand, inert DT alkane chains behave as physical spacers between the particles and the titania shell. In nanoparticles containing only MPMS, a silica layer is formed around the gold nanoparticle, making its surface inaccessible for catalysis. On the other hand, without MPMS the titania mesoporous structure would grow independently of gold nanoparticles.[6]

To further control the Ti-Ti and Ti-Au distance in the Au-organic-Ti mesoporous structures, we used rigid carboxylic acid as spacers in between titanium centers (Scheme 1). Three carboxylates with different lengths were tested in the present work: terephtalic acid, 2,6-naphthalenedicarboxylic acid and 1,3,5-tris(4-carboxyphenyl)benzene. The use of such organic compounds initially resulted in highly porous organic-inorganic hybrid frameworks resembling those of metal organic frameworks.[13-15]

Figure 2 shows the IR spectra of the isolated free acid (Fig. 2A) and the hybrid material (Fig. 2B). The carboxylate stretching frequencies are between 1600-1380 cm^{-1}. Bands around 1400 cm^{-1} correspond to symmetric stretching modes γ_{sym} and bands between 1600-1500 cm^{-1} are assigned to asymmetric modes γ_{asym}. The difference between carboxylate stretching frequencies $\Delta = \gamma_{asym}-\gamma_{sym}$ of the ionic therephtalic structure is around Δ=177cm^{-1}.[10] We suppose similar values for the other ionic structures. We determined the bonding mode between the carboxylic acids groups and titanium centers in Au-organic-Ti structures by measuring $\Delta=\gamma_{asym}-\gamma_{sym}$. While monodentate complexes have higher Δ values than the ionic structure, in bidentate-bridging modes Δ values are lower but close to the ionic value, and bidentate chelating modes exhibit much lower Δ values than the corresponding ionic structure.[10,16] The frequency separations compiled in Table 2 suggests that terephthale and 1,3,5-tris(4-carboxyphenyl)benzene ligands were bonded to titanium as a monodentate and bidentate-chelating mode. However, 2,6-naphthalenedicarboxylic was bonded in the bidentate-bridging and chelating bridging mode.

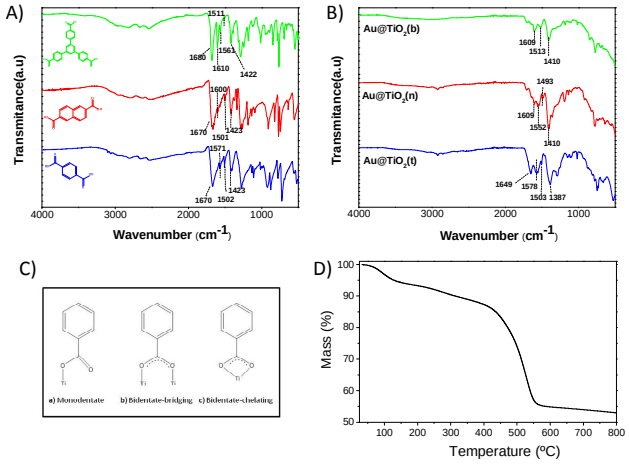

Figure 2. IR spectra of the isolated free acid (a) and the hybrid material (b). c) carboxylate coordination modes. d) Thermogravimetric profile of the Au@TiO_2(t) mesoporous materials.

Table 2. Difference stretching frequencies of the isolated free acid and the hybrid material.

Carboxylate	$\Delta=\gamma_{asym}-\gamma_{sym}$ cm^{-1}		*Bonding mode*
	Free acid	*Hybrid material*	
Terephtalic	247	199-116	Monodentate-bidentate
2,6-Naphthalenedicarboxylic	247	142-83	Bidentate-chelating
1,3,5-Tris(4-carboxyphenyl)benzene	258	191-103	Monodentate-bidentate

To determine the temperature required for organic removal, thermogravimetry analyses were conducted. Samples were heated at a rate of 10 °C·min^{-1} from room temperature to 800 °C in air

(Figure 2d). Three weight loss steps were detected in most samples. The first weight loss step, in the range from 50 to 200 °C, was associated with the evaporation of adsorbed water and weakly bonded solvent molecules. A second weight loss step, in the range 200-400 °C, was associated with the desorption of residual diethylformamide and interstitial water. The last step, starting at 450 °C, corresponds to the pirolysis of the organic molecules, such as DT, MPMS and the organic spacers.

Elemental analysis showed a calcination treatment at 450 ºC during 4h to be sufficient to totally remove the organic spacers. Therefore all the materials were calcined at 450 °C during 4 hours in air. The powder obtained was white for the samples with no Au and reddish-violet for the Au@TiO_2 samples. ICP revealed the Au content after calcination to be around 1% for all samples prepared.

Figure 1b displays a TEM micrograph of the Au@TiO_2(t) mesoporous material finally obtained. Embedded Au nanoparticles were hardly seen due to their small size, high dispersion and relatively low concentration. However, few large Au nanoparticles independent to the TiO_2 matrix were also observed. These large Au particles may be originated from initial gold aggregates which were not properly functionalized and thus were not embedded inside the TiO_2 structure.

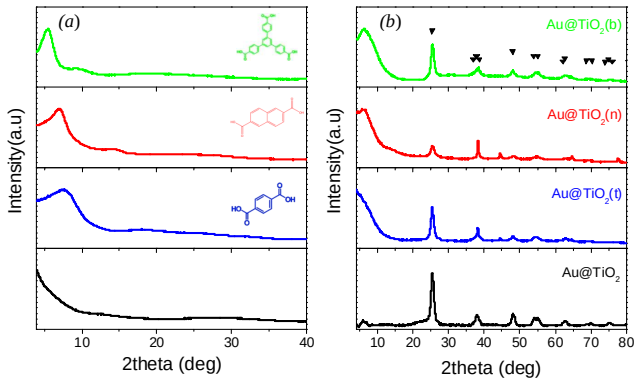

Figure 3. X-ray diffraction patterns from the different Au@TiO_2 mesoporous structures before (a) and after (b) the calcination treatment. The peaks corresponding to the anatase phase are marked as a reference.

Figure 3 shows the XRD patterns of the Au-spacer-Ti mesoporous materials initially obtained. No diffraction peak from the titania crystallographic structure was detected in the as-prepared materials, proving its amorphous nature. However, the presence of x-ray reflections at low angles indicated some degree of structural organization at the nanometer scale. The diffraction peaks of the Au-spacer-Ti materials were shifted to lower angles with increasing the size of the organic carboxylate. Table 3 displays the d-spacing values calculated using the Bragg law. The increase of the d-spacing with the size of the carboxylate molecule correlates well with the picture of Ti atoms separated by the different organic linkers.

With the calcination treatment the titania support crystallized into the anatase phase (JCPDS 21-1272, Figure 3b). When using organic spacers, a small peak at 30.8º corresponding to the brookite phase was also identified. The TiO_2 crystallite size was estimated at 9-10 nm from the full width at half maximum of the (011) peak by Scherrer's equation.[17] This reduced particle size potentially favor the catalytic performance of the material, as it increases the density of metal-support active-sites.[1,18-20].

Table 3. Surface area before and after calcination and position of the main XRD peak of the as-prepared sample.

Sample name	Carboxylate	XRD spacing d (nm)	Surface area (m^2/g)		Pore size(Å)
			As-prepared	*Calcined*	
TiO_2	-	-	552	64	53
TiO_2(t)	Terephtalic acid	1.14	226	85	155
TiO_2(n)	2,6-naphthalenedicarboxylic acid	1.24	176	153	160
TiO_2(b)	1,3,5-Tris(4-carboxyphenyl)benzene	1.61	341	180	42
Au@TiO_2	-	-	349	89	55
Au@TiO_2(t)	Terephtalic acid	1.13	293	109	280
Au@TiO_2(n)	2,6-Naphthalenedicarboxylic acid	1.37	183	178	328
Au@TiO_2(b)	1,3,5-Tris(4-carboxyphenyl)benzene	1.90	314	145	514

Figure 4 shows the adsorption-desorption isotherm N_2 cycles of the materials produced. The specific surface area of the as-prepared Au-spacer-Ti mesoporous materials was in the range between 150 and 350 m^2/g. They showed type IV-H1 adsorption-desorption isotherm cycles. Their porous contribution was essentially mesoporous, and they displayed broad BJH pore size distributions (Figure 4c, Supporting Information). The as-prepared Au-Ti materials, with no spacer, typically displayed BET surface areas close to 350 m^2g^{-1} (Table 3) and type IV-H4 adsorption-desorption isotherms. TiO_2 materials produced in the same way but without Au nanoparticles were characterized by larger BET surface areas, above 550 m^2/g. These samples, having no gold and no spacer, presented type I physisorption isotherms, characteristic of microporous materials.[21,22]

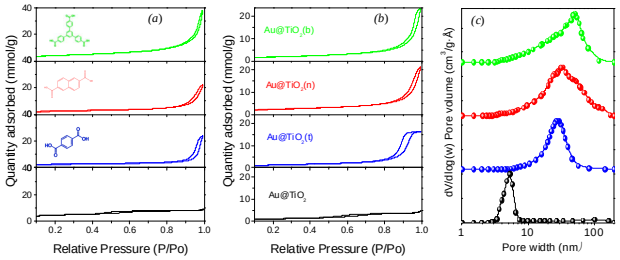

Figure 4. a), b): Adsorption/desorption isotherm cycles from the different Au@TiO_2 mesoporous structures before (a) and after (b) the calcination treatment. c) BJH pore size distribution of the materials after calcination.

After calcination, the isotherms of all Au@TiO_2 materials conserved the characteristic type IV cycles corresponding to mesoporous materials. However, a decrease of the surface area was obtained. Larger spacers had associated smaller surface area decreases, being the largest surface area decrease observed for the materials with no organic spacer. We believe that the higher thermal stability of the larger carboxylate molecules more

effectively prevented the mesoporous structure to collapse. This is consistent with the picture of organic spacer as effective structural directors.

Owing to its largest surface area, we selected the catalyst Au@TiO_2(b), prepared using 1,3,5-tris(4-carboxyphenyl)benzene acid as spacer, to compare the catalytic activity of embedded Au@TiO_2 materials with that of impregnated samples. The impregnated Au/TiO_2 sample was prepared by impregnating a mesoporous TiO_2 materials obtained using the 1,3,5-tris(4-carboxyphenyl)benzene spacer with 1% of Au: Au/TiO_2 (b). As a reference, we also measured the catalytic performance of Au@TiO_2 without spacer and that of the TiO_2 sample with no gold, TiO_2(b).

The materials catalytic activity was tested through the CO oxidation reaction in the temperature range from 25 ºC to 250 °C (Figure 5).[23-28] At each temperature, the system was allowed to stabilize during 10 min. Au@TiO_2(b) showed CO to CO_2 conversions above 80 % at 50 °C and close to 100 % at temperatures above 100 °C. The sample with no spacer showed lower catalytic conversion. Au@TiO_2 showed 25 % CO to CO_2 conversion at 50 ºC and above 70 % at 250 ºC. These results probed the presence and accessibility of nanometric and active gold nanoparticles within the Au@TiO_2(b) and Au@TiO_2 mesoporous materials and confirmed that the use of spacers increased the accessibility of the catalytic materials inside the TiO_2 network. On the contrary, TiO_2(b) and impregnated Au/TiO_2(b) samples showed a very reduced catalytic activity in the temperature range tested, most probably due to the limited availability of metal catalyst nanoparticles with small enough sizes.

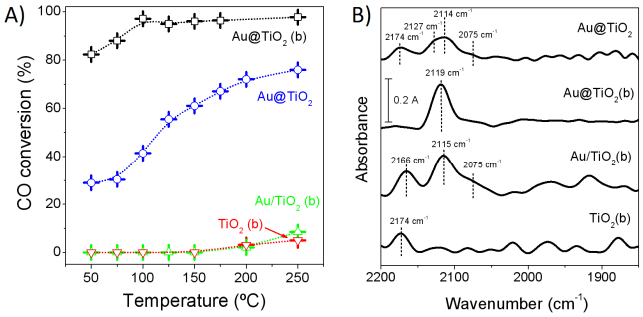

Figure 5. A) CO conversion as a function of temperature for pure TiO_2 support, impregnated Au/TiO_2(b), embedded Au@TiO_2 and Au@TiO_2(b). B) DRIFT spectra under CO oxidation reaction

We further studied the materials catalytic performance using DRIFT spectroscopy coupled to mass spectrometry to follow the evolution of adsorbed species. Before the CO-O_2 adsorption experiment, samples were treated at 150 °C in oxygen atmosphere. At this temperature, CO and oxygen were introduced into the DRIFT chamber. After 1h, the reaction was quenched by introducing He into the chamber and quickly cooling the material to 25 °C. During cooling, free CO and CO_2 progressively disappeared but bonded CO remained attached to the material surface. Figure 5b shows the DRIFT spectra after quenching. The TiO_2(b) support showed a unique band at 2174 cm^{-1} assigned to CO adsorbed to Ti^{IV} sites on the anatase surface.[29-31] Au@TiO_2 and impregnated Au/TiO_2(b) samples presented various CO coordination sites: i) a band centered at 2174-2166 cm^{-1} resembled the band obtained for the TiO_2(b) support; ii) a small band located at 2075 cm^{-1} was assigned to CO adsorbed on low coordinated Au^o species; iii) a band centered at 2114-2115 cm^{-1} and possibly a shoulder at 2127 cm^{-1} detected only for Au@TiO_2 were assigned to CO adsorbed on slightly positively charged gold atoms, $Au^{\delta+}$, characteristic of Au-O-Ti bonds at the metal-support interface.[29-31] Au@TiO_2(b) displayed just this last unique and well defined coordination site characterized by a band located at 2119 cm^{-1}.

The water gas shift (WGS) reaction was also studied using the Au@TiO_2(b) catalyst. For this reaction, the calculated turnover frequency value after 6 h reaction at 250 °C was $6.8 \cdot 10^7$ $molH_2/molAu \cdot s$. This result confirmed that nanometric gold nanoparticles within Au@TiO_2(b) had optimal size for the water−gas shift reaction.[32-34]

Conclusions

A general procedure to prepare high surface area materials with highly dispersed and accessible embedded catalytic nanoparticles was described. The use of organic spacers as linkers between Ti atoms allowed producing hybrid organic-inorganic structures with tuned porosity. The final mesoporous materials efficiently blocked the aggregation and growth of the gold nanoparticles, minimizing their sintering during the calcination treatment and increasing the interaction strength between the metal nanoparticles and the oxide support. The good accessibility of gold nanoparticles in these materials was demonstrated by the high CO to CO2 conversion values obtained at low temperatures. DRIFT spectroscopy showed a well-defined and specific coordination sites on Au@TiO_2(b) catalyst related to $Au^{\delta+}$ species resulting from Au-O-Ti interactions at the metal support interface.

The same strategy can be used to prepare other mesoporous supports starting from the corresponding alkoxides, e.g. CeO_2, Fe_2O_3, Al_2O_3. At the same time other metal nanoparticles can be introduced in these materials. The only requirement is the proper functionalization of their surface. This opens the door to produce a large variety of catalytic materials containing highly dispersed and accessible metal nanoparticles with controlled size, shape and composition prepared by colloidal synthesis techniques.

Acknowledgements

The research was supported by the European Regional Development Funds and the Spanish MICINN projects CSD2009-00050, MAT2011-29020-C02-01 and Severo Ochoa Excellence Program SEV-2012-0267.

Notes and references

[a] Catalonia Institute for Energy Research, IREC, Sant Adrià del Besos, Barcelona, 08930, Spain

[b] Departament de Química Inorgànica, Universitat de Barcelona, Barcelona, 08028, Spain

[c] Departament d'Electrònica, Universitat de Barcelona, Barcelona, 08028, Spain
[d] Instituto de Tecnología Química (UPV-CSIC), Universidad Politécnica de Valencia, Avenida de los Naranjos s/n 46022 Valencia, Spain.
Corresponding author: acabot@irec.cat ; acorma@itq.upv.es

1. C. J. Jia, F. Schüth, *Phys. Chem. Chem. Phys., 2011*, **13**, 2457–2487.
2. T. Herranz, X. Deng, A. Cabot, J. Guo, M. Salmeron, *J. Phys. Chem. B.*, 2009, **113**, 10721–10727.
3. T. Herranz, X. Deng, A. Cabot, P. Alivisatos, Z. Liu, G. Soler-Illia, M. Salmeron, *Catal. Today*, 2009, **143**, 158–166.
4. T. Herranz, X. Deng, A. Cabot, Z. Liu, M. Salmeron, *J. Catal.*, 2011, **283**, 119–123.
5. C. Flox, J. Rubio-García, R. Nafria, R. Zamani. M. Skoumal. T. Andreu, J. Arbiol, A. Cabot, J. R. Morante, *Carbon., 2012*, **50**, 2372-2374.
6. G. Budroni, A. Corma, *Angew. Chem. Int. Ed., 2006,* **45**, 3328–3331.
7. G. Budroni, A. Corma, H. García, A. Primo, *J. Catal., 2007*, **251**, 345–353.
8. B. Rodríguez-González, V. Salgueiriño-Maceira, F. García-Santamaría, L. M. Liz-Marzán., *Nano Lett., 2002*, **2**, 471–473.
9. Y. Kobayashi, M. A. Correa-Duarte, L. M. Liz-Marzán, *Langmuir*, 2001, **17**, 6375–6379.
10. M. Sabo, W. Böhlmann, S. Kaskel, *J. Mater. Chem.*, 2006, **16**, 2354.
11. X. Li, X. Liu, Y. Yang, J. Zhao, C. Li, Q. Yang**,** *J. Mater. Chem.*, 2012, **22**, 21045–21050.
12. N. M. Wichner, J. Beckers, G. Rothenberg, H. Koller, *J. Mater. Chem.*, 2010, **20**, 3840–3847.
13. S. Hausdorf, J. Wagler, R. Mossig, F. O. R. L, Mertens, *J. Phys. Chem. A.*, 2008, **112**, 7567–7576.
14. S. Hausdorf, F. Baitalow, J. Seidel, F. O. R. L. Mertens, *J. Phys. Chem. A.*, 2007, **111**, 4259–4266.
15. M. Dan-Hardi, C. Serre, T. Frot, L. Rozes, G. Maurin, C. Sanchez, G. Férey, *J. Am. Chem. Soc.*, 2009, **131**, 10857–10859.
16. S. W. Boettcher, M. H. Bartl, J. G. Hu, G. D. Stucky, *J. Am. Chem. Soc.*, 2005, **127,** 9721–9730.
17. P. Scherrer, Göttinger Nachrichten, 1918, **2**, 90.
18. J. C. Fierro-Gonzalez, B. C. Gates, *Chem. Soc. Rev.*, 2008, **37**, 2127.
19. Z. Ma, S. Dai, *Nano Res.*, 2011, **4**, 3–32.
20. J. C. Fierro-Gonzalez, B. C. Gates, *Catal. Today*, 2007, **122**, 201–210.
21. K. S. W. Sing, *Pure Appl. Chem.*, 1985, **57**, 603–619.
22. V. Meynen, P. Cool, E. F. Vansant, *Microporous Mater.*, 2009, **125**, 170–223.
23. J. J. Pietron, R. M. Stroud, D. R. Rolison, *Nano Lett.*, 2002, **2**, 545–549.
24. H. Zhu, Z. Ma, S. H. Overbury, S. Dai, *Catal. Lett.*, 2007 **116**, 128–135.
25. Y. Denkwitz, J. Geserick, U. Hörmann, V. Plzak, U. Kaiser, N. Hüsing, R. J. Behm, *Catal. Lett.*, 2007, **119**, 199–208.
26. R. Zanella, V. Rodríguez-González, Y. Arzola, A. Moreno-Rodriguez, *ACS Catal.*, 2012, **2,** 1–11.
27. S. Carrettin, P. Concepción, A. Corma, A. J. M. López Nieto, V. F. Puntes, *Angew. Chem. Int. Ed.*, 2004, **43**, 2538–2540.
28. M. M. Schubert, S. Hackenberg, A. C van Veen, M. Muhler, V. Plzak, R. J. Behm, *J. Catal.*, 2001, **197**, 113–122.
29. M. Boronat, P. Concepción, A. Corma, *J. Phys. Chem. C.*, 2009, **113**, 16772–16784.
30. I. X. Green, W. Tang, M. Neurock, J. T. Yates, *Science*, 2011, **333**, 736–739.
31. M. Raphulu, J. McPherson, E. Van der Lingen, J. Anderson, M. Scurrell, *Gold Bulletin*, 2010, **43**, 334–344.
32. T. Si, J. Tao, J. Evans, J. B. Park, L. Barrio, J. C. Hanson, Y. Zhu, J. Hrbek, J. A. Rodriguez, *J. Phys. Chem.*, 2012, **116**, 23547−23555.
33. M. Yang, L. F. Allard, M. Flytzani-Stephanopoulos, *J. Am. Chem. Soc.*, 2013, **135**, 3768–3771.
34. J. Wang, V. F. Kispersky, N. W. Delgass, F. H. Ribeiro, *J. Catal.*, 2012, **289**, 171–178.

